HHS Public Access

Author manuscript

Neuroimage. Author manuscript; available in PMC 2016 February 15.

Published in final edited form as:

Neuroimage. 2015 February 15; 107: 229–241. doi:10.1016/j.neuroimage.2014.10.039.

Optogenetic fMRI reveals distinct, frequency-dependent networks recruited by dorsal and intermediate hippocampus stimulations

Andrew J. Weitz[a,†], **Zhongnan Fang**[b,c,†], **Hyun Joo Lee**[c,d,†], **Robert S. Fisher**[d,†], **Wesley C. Smith**[e,†], **ManKin Choy**[d], **Jia Liu**[e,f], **Peter Lin**[c,d], **Matthew Rosenberg**[g], and **Jin Hyung Lee**[a,b,c,d,e,f,h,*]

[a]Department of Bioengineering, Stanford University, CA 94305, USA

[b]Department of Electrical Engineering, Stanford University, Stanford, CA 94305, USA

[c]Department of Electrical Engineering, University of California, Los Angeles, CA 90095, USA

[d]Department of Neurology and Neurological Sciences, Stanford University, CA 94305, USA

[e]Neuroscience Interdepartmental Program, University of California, Los Angeles, CA 90095, USA

[f]Department of Psychiatry and Biobehavioral Sciences, University of California, Los Angeles, CA 90095, USA

[g]Department of Psychology, University of California, Los Angeles, CA 90095, USA

[h]Department of Neurosurgery, Stanford University, CA 94305, USA

Abstract

Although the connectivity of hippocampal circuits has been extensively studied, the way in which these connections give rise to large-scale dynamic network activity remains unknown. Here, we used optogenetic fMRI to visualize the brain network dynamics evoked by different frequencies of stimulation of two distinct neuronal populations within dorsal and intermediate hippocampus. Stimulation of excitatory cells in intermediate hippocampus caused widespread cortical and subcortical recruitment at high frequencies, whereas stimulation in dorsal hippocampus led to

*Correspondence to: Jin Hyung Lee, PhD, ljinhy@stanford.edu, 1201 Welch Road, #P206, Stanford, CA 94305, (650) 736-2069.
†These authors contributed equally.

Author Contributions

A.J.W. conducted data processing and analysis, performed EEG experiments, helped make the figures, obtained optical microscopy images, and wrote the paper. Z.F. implemented the data acquisition system, developed the data analysis software, and helped make the figures and videos. H.J.L. conducted EEG probe implantations and performed video-EEG experiments. W.C.S. conducted surgeries, fMRI experiments, and video-EEG experiments. M.C. scored the EEG and behavioral video data, performed pilocarpine experiments, and helped write the paper. J.L. helped reconstruct the images. P.L. helped with the behavioral experiments. M.R. constructed the behavioral test chamber and helped conduct the behavioral experiments. R.S.F. provided expertise on animal models of epilepsy, scored the EEG and behavioral video data, and helped write sections of the paper. J.H.L. designed and planned all experiments, supervised and organized the study, analyzed and interpreted data, wrote the paper, and outlined the figures and videos.

activity primarily restricted to hippocampus across all frequencies tested. Sustained hippocampal responses evoked during high-frequency stimulation of either location predicted seizure-like afterdischarges in video-EEG experiments, while the widespread activation evoked by high-frequency stimulation of intermediate hippocampus predicted behavioral seizures. A negative BOLD signal observed in dentate gyrus during dorsal, but not intermediate, hippocampus stimulation is proposed to underlie the mechanism for these differences. Collectively, our results provide insight into the dynamic function of hippocampal networks and their role in seizures.

Keywords

functional MRI; brain mapping; optogenetics; hippocampus; seizure

1. Introduction

Based on a large volume of anatomical, behavioral, and genetic data, it has been argued that the dorsal and intermediate compartments of the hippocampus are two functionally distinct regions (Fanselow and Dong, 2010). This claim is supported by observations of differences along the dorsoventral axis of the hippocampus, including the distribution of cortical afferents and projections (Cenquizca and Swanson, 2007; de No, 1934; Van Groen and Lopes da Silva, 1985), connections with other subcortical structures (van Groen and Wyss, 1990), commissural and intrinsic connections (van Groen and Wyss, 1990), neurochemical makeup (Garcia Ruiz et al., 1993; Tanaka et al., 2012), and cell morphology (Dong et al., 2009). In addition to these physical differences, physiological properties such as spatial field tuning (Jung et al., 1994), vulnerability to ischemia (Ashton et al., 1989), and evoked field potential responses (Gilbert et al., 1985) also differ along the dorsoventral axis. Furthermore, lesion, stimulation, and pharmacological studies have demonstrated distinct behavioral effects when different areas along this axis are targeted (Hock and Bunsey, 1998; Siegel and Flynn, 1968). Nevertheless, despite the wealth of information on these differences, exactly how they contribute to large-scale functional network activity remains unknown. Furthermore, less is known about the intermediate hippocampus, with most studies focusing on the dichotomy between dorsal and ventral regions. We chose to target the intermediate, rather than ventral, hippocampus to study how network properties differ with small changes in distance along the dorsoventral axis.

While anatomical connectivity provides a foundation for studying a region’s functional role in neural circuits, understanding how projections translate to activity is best done by directly manipulating the population of interest and observing the downstream effects. Electrical stimulation was traditionally used for this purpose (Canals et al., 2009; Canals et al., 2008), but the recent development of optogenetics has enabled greater precision in the temporal pattern of excitation and the specific subset of neurons targeted (Boyden et al., 2005; Yizhar et al., 2011; Zhao et al., 2011). Electrophysiology measurements have typically been used to observe downstream effects of stimulation, but are limited by a finite number of recording sites, requiring *a priori* hypotheses about which regions are affected. As one of the few modalities that can report activity across the entire brain with relatively high spatial resolution, functional magnetic resonance imaging (fMRI) offers a viable alternative to

studying the network-level behavior of neural circuits in both humans and small animals (Bullmore and Sporns, 2009; Goloshevsky et al., 2008; Huettel et al., 2004; Yu et al., 2010). By measuring the blood oxygenation-level dependent (BOLD) signal over time, fMRI provides an indirect measure of neuronal activity, including both spatial and temporal dynamics (Kim et al., 2004).

Optogenetic functional magnetic resonance imaging (ofMRI) is a novel technology that combines the precision of optogenetic stimulation with the whole-brain readout capability of fMRI (Desai et al., 2011; Lee, 2011, 2012; Lee et al., 2010; Vazquez et al., 2013; Weitz and Lee, 2013). Unlike fMRI experiments with cognitive, sensory, or even direct electrical stimuli, ofMRI can investigate the brain's response to a cell type-specific population being driven in a temporally precise manner, revealing important aspects of a network's connectivity and frequency response *in vivo*. This has enabled investigators, for the first time, to manipulate specific elements of a neural circuit with precision in an intact animal and observe the causal flow of activity within the global brain circuit. By systematically investigating different patterns of input and measuring the brain's response, a region's functional and dynamic connectivity can be characterized. In particular, this technique can be used to investigate how network activity changes with different temporal patterns of input. Several studies employing optogenetics have already demonstrated the distinct frequency responses that neuronal circuits can exhibit (Adamantidis et al., 2007; Carter et al., 2010; Gradinaru et al., 2009). Although several experiments have used ofMRI to examine the functional connectivity of different regions (Abe et al., 2012; Desai et al., 2011; Lee et al., 2010), this aspect of neuronal dynamics has not been explored yet. In addition, several other questions remain unanswered. Can ofMRI detect activity across multiple synapses? Can it dissociate inhibitory and excitatory activities? And can it reveal the spatiotemporal dynamics of large-scale, multi-region networks?

In the present study, we sought to address these issues by using high-resolution, high-field ofMRI to investigate the causal, frequency-dependent network activity driven by CaMKIIa-positive cells in dorsal (DH) and intermediate (IH) hippocampus of rats. CaMKIIa-positive cells in these two regions were selectively stimulated using optogenetic techniques at 6, 10, 20, 40, and 60 Hz during whole-brain fMRI scans. Our results indicate distinct networks recruited by stimulation of either region in a frequency-dependent manner, and point to the potential of ofMRI in uncovering the functional significance of each region in large-scale neuronal networks and behavior.

2. Materials and Methods

2.1 Subjects

Adult male Sprague-Dawley rats (250–350 g; Charles River Laboratories, Wilmington, MA) were used as subjects. Animals were individually housed under a 12-hour light-dark cycle and provided with food and water *ad libitum*. Animal husbandry and experimental manipulation were in strict accordance with National Institute of Health, UCLA Institutional Animal Care and Use Committee (IACUC), and Stanford University IACUC guidelines.

2.2 Surgical Preparations

To achieve targeted control of a single neuronal population in the dorsal or intermediate hippocampus, we injected adeno-associated virus expressing a Channelrhodopsin2-EYFP (enhanced yellow fluorescent protein) fusion protein under control of the Ca^{2+}/calmodulin-dependent protein kinase IIa (CaMKIIa) promoter (expressed primarily in excitatory cells) into either region of the right hemisphere. The pAAV-CaMKIIa-ChR2(H134R)-EYFP plasmid was constructed by cloning CaMKIIa-ChR2(H134R)-EYFP into an AAV backbone using MluI and EcoRI restriction sites (map available online at www.optogenetics.org). The recombinant AAV vector was serotyped with AAV5 coat proteins and packaged by the University of North Carolina viral vector core (titer of 2×10^{12} particles/mL).

During surgery, rats were anesthetized with isoflurane (induction 5%, maintenance 2–3%; Sigma-Aldrich) and secured in a stereotactic frame. Following a midline incision, a small craniotomy and viral injection/cannula implantation were performed at the dorsal hippocampus (−4.3 mm AP, +1.2 mm ML right hemisphere, −3.1 mm from bregma; Fig. 1A,B) or intermediate hippocampus (−5.8 mm AP, +5.2 mm ML right hemisphere, −3.4 mm from bregma; Fig. 1C,D). 2 uL of virus were delivered through a 34-gauge needle (World Precision Instruments Inc.) at 150 nl/min. The syringe needle was left in place for ten minutes before being slowly withdrawn. A custom-designed fiber optic cannula was mounted and secured on the skull using metabond (Parkell Inc.), with the fiber optic's end positioned 0.2 mm above the corresponding injection site to ensure adequate illumination of transfected cells. Incisions were sutured, and animals were kept on a heating pad until recovery from anesthesia. Buprenorphine was injected subcutaneously twice daily for 48 hours post-operatively to minimize discomfort. All experiments were conducted at least 3 weeks after virus injection to allow for optimal ChR2 expression.

Upon completion of ofMRI studies, a cohort of the imaged animals underwent additional surgeries for EEG electrode implantation (n = 3 DH-injected; n = 4 IH-injected). Surgical preparation details were the same as those used for virus injection and cannula placement. Two stainless steel screws (0–80, 1.5 mm diameter, Plastics One Inc.) were attached to ~2 cm of insulated wire (30 gauge, R30Y0100, Wire Wrapping Wire, O.K. Industries) and affixed to the skull over the frontal cerebral cortex (Fig. S1 A). A reference electrode was placed approximately 3 mm anterior and 2 mm to the right of bregma. The recording electrode was placed at the edge of the cerebral cortex above the dorsal or intermediate hippocampus approximately 1.5 mm caudal to the optical fiber implant location. Electrodes were mounted on the skull and secured with metabond (Parkell Inc.). Incisions were closed with 5-0 nylon skin sutures. Surgical recovery details were the same as those for virus injection. Animals were also supplied with trimethoprim-sulfamethoxazole antibiotic (48 mg/100 ml) in their water.

2.3 of MRI Experiments

fMRI scanning was performed in a 7T Bruker Biospec small animal MRI system at UCLA. Animals were initially anesthetized with 5% isoflurane and intubated before placement onto custom-made MRI-compatible cradles. Intubation was performed according to a protocol from Rivard et al. (Rivard et al., 2006) by inserting a modified 16- or 18-gauge i.v. catheter

into the glottis to serve as an endotracheal tube. A 39 mm outer diameter, 25 mm inner diameter custom-designed transmit/receive single-loop surface coil was centered over the region of interest on the skull to maximize signal-to-noise ratio. An optical fiber of 62.5 μm core diameter was connected to a 473 nm laser source and coupled with the implanted cannula.

During fMRI scanning, animals were placed into the iso-center of the magnet while artificially ventilated (45–55 strokes/min) under light anesthesia using a ventilator (Harvard Apparatus, Model 683 Small Animal Ventilator) and calibrated vaporizer with a mixture of O_2 (35%), N_2O (63.5%), and isoflurane (1.2–1.5%). Expiratory CO_2 was kept at 3–4%, and body temperature was maintained at 36–38 °C using heated airflow. T2-weighted high-resolution anatomical images were acquired prior to fMRI scanning to check for brain damage and validate the optical fiber's location. Gradient recalled echo (GRE) BOLD methods were used to acquire fMRI images during photostimulation. The fMRI image acquisition was designed to have 35×35 mm^2 in-plane field of view (FOV) and 0.5×0.5×0.5 mm^3 spatial resolution with a sliding window reconstruction to update the image every repetition time (TR) (Fang and Lee, 2013). The two-dimensional, multi-slice gradient-echo sequence used a four-interleave spiral readout (Glover and Lee, 1995; Kim et al., 2003), 750 ms TR, and 12 ms echo time, resulting in 23 coronal slices. The spiral k-space samples were reconstructed through a 2-dimensional gridding reconstruction method (Jackson et al., 1991). Finally, real-time motion correction was performed using a custom-designed GPU-based system (Fang and Lee, 2013).

A single ofMRI scan consisted of six 20 s pulse trains of light (6, 10, 20, 40, or 60 Hz, tested in randomized order) delivered once per minute over 6 minutes. This stimulation paradigm was chosen because it had previously been shown to reliably evoke detectable hemodynamic response functions with optogenetic stimulation (Lee et al., 2010). Stimulation frequencies were chosen to cover the range over which action potentials can be consistently evoked (Mattis et al., 2012), and to compare with earlier optogenetic studies using a similar frequency range (Osawa et al., 2013). A duty cycle of 30% was used across frequencies to maintain the total amount of light delivery. Control scans were also collected with saline-injected animals (one per injection site) using identical stimulation and imaging parameters for 6, 20, 40, and 60 Hz. For all experiments, the optical fiber output power was measured to be between 2.5 and 3 mW. Assuming that 1 mW/mm^2 is required for ChR2 activation (Aravanis et al., 2007), 3 mW power corresponds to a maximum tissue volume of 0.022 to 0.083 mm^3 directly activated by photostimulation for our specific fiber (0.275 numerical aperture, http://www.optogenetics.org/).

2.4 fMRI Data Analysis

All fMRI data processing was performed using custom-written programs and mrVista (Stanford Vision and Imaging Science and Technology Laboratory) in Matlab (MathWorks, Inc.). Motion-corrected images belonging to consecutive scans of the same stimulation paradigm were first averaged together. The average 4D images were then aligned to a common coordinate frame, using a six degree-of-freedom rigid body transformation plus

isotropic scaling. If multiple scanning sessions were performed on the same animal at the same frequency, these images were also averaged together.

Time series were calculated for each voxel in these individual-animal datasets as the percent modulation of the BOLD signal relative to a 30 s baseline period collected prior to stimulation. Activated voxels were identified as those whose time series were significantly synchronized to multiple blocks of optical stimulation using the quantity of coherence. A coherence value was calculated for each voxel's time series as the magnitude of its Fourier transform at the frequency of repeated stimulation cycles (i.e. 1/60 Hz) divided by the sum-of-squares of all frequency components (Engel et al., 1997; Lee et al., 2010). This analysis detects signals that are synchronized to the 20 s on / 40 s off (60 s total) block design employed in our experiments. Active voxels were identified as those with a coherence greater than 0.35. Assuming Gaussian noise, the *P* value for a given coherence threshold can be estimated (Bandettini et al., 1993) as:

$$p=1-f_e(c\times\sqrt{N/2})$$

where f_e represents the error function, c is the chosen coherence value, and N is the number of points in the time series (N = 480 for our experiments). Applying a Bonferroni correction for all brain-masked voxels, the *P* value threshold for our analyses is less than 10^{-9}. For the analysis in Figure 5, a coherence threshold of 0.25 was used to account for lower functional SNR. This corresponds to a *P* value threshold of 0.0015.

Time series and hemodynamic response functions (HRFs) used for figures were generated by averaging the mean time series or mean HRF of active voxels in the prescribed region of interest (ROI) across animals. Because some animals had more robust activity than others in certain regions, only images with at least 10 active voxels in the prescribed ROI were included. This ensured that very weak responses that could not be quantified were excluded from analysis. ROIs were defined by aligning a T2-weighted anatomical scan coregistered with the functional images with a digital standard rat brain atlas (Paxinos and Watson, 2006). HRFs were calculated as the average 60 s response of a voxel's six-cycle time series or a group of voxel's average six-cycle time series. The first data point of each HRF was subtracted as a baseline offset to define the signal's relative percent modulation from the onset of stimulation.

To analyze the temporal dynamics of each voxel, the duration of its response was calculated as the amount of time for which its boxcar-filtered HRF stayed above 40% of its maximum value. To improve the accuracy of this quantification, a voxel was discarded if its HRF did not exceed the 40% value for at least 4 consecutive time points (3 s). To objectively identify negative BOLD responses, we used the phase of the Fourier transform of each voxel's time series at the frequency of repeated stimulations (1/60 Hz). This represents the temporal shift of the response when it is modeled as a sinusoid. Negative responses were classified as those having a phase between 0.9π and 1.3π, which is the approximate range over which the sinusoidal response during stimulation is negative.

To generate activation maps and cross-correlation matrices, the 4D fMRI images from experiments at the same stimulation location and frequency were normalized and averaged together across animals for group analysis. These datasets were then processed according to the above Fourier domain analyses. To visualize activation patterns, thresholded coherence maps were overlaid onto a corresponding T2-weighted anatomical scan from a DH- or IH-injected animal and masked with the digital standard rat brain atlas used for ROI segmentation (Paxinos and Watson, 2006). Seven animals were averaged for each DH stimulation frequency, except 6 Hz (n = 4). Eight animals were averaged for each IH stimulation frequency, except 6 Hz (n = 5) and 40 Hz (n = 7). Not all animals were scanned at each of the five frequencies, which accounts for these differences.

Signal-to-noise ratio (SNR) maps were computed for the last frame acquired before stimulation as $SNR_i = 20*\log_{10}(M_i/\sigma)$, where M_i is the i^{th} voxel's signal intensity and σ is the background variance estimated using the method of moments (Henkelman, 1985; Sijbers et al., 1998) according the equation shown below. Here, N is the number of background points used for estimation.

$$\sigma^2 = \frac{1}{2N}\sum_{j=1}^{N} M^2{}_j$$

2.5 EEG and Behavioral Experiments

A custom-designed behavioral chamber with three video cameras was used for video-EEG recordings (Fig. S1B). Animals were acclimated to the chamber, and received food and water between trials. A commercial digital EEG system (Biopac MP 150 & MEC100C) was used with a sampling rate of 1 kHz per channel. All animals were stimulated in an awake state, as verified by movement in the recorded video or - in cases where movement was not clearly observed -subsequent EEG power spectrum analysis. For each video-EEG trial, baseline EEG recordings were collected for 5 min, followed by 20 s of photostimulation every 5 min for 15 min. Up to five frequencies of stimulation (6, 10, 20, 40, and 60 Hz) were tested in each animal in randomized order.

To perform control experiments (n = 2 DH-injected; n = 4 IH-injected animals), two fiber optic cables were used: one attached to the implanted cannula (stimulation), and one affixed to the ferrel but not attached to the cannula (no stimulation). Light was delivered from a single source to both cables during normal experiments, but only to the cable outside of the cannula during control experiments. Because the ferrel was always covered, any light that escaped appeared equally bright between the two conditions. No changes in EEG activity or behavior were observed during these control experiments, confirming that visual stimuli did not cause the responses observed in experimental trials.

All video-EEG recordings were scored blindly, post-collection by an experienced rat electroencephalographer. EEG recordings were manually read using commercial EEG analysis software (Biopac AcqKnowledge ver. 4.4.1) to determine if an evolving electrographic seizure occurred based on the observation of stereotyped waveforms, and – if so – the duration of the afterdischarge. Afterdischarge duration was measured as the time

between the end of stimulation and the point at which the EEG response returned to baseline conditions. Video recordings paired to each EEG were used to classify the behavioral response according to a modified Racine scale for seizures: 1) no overt behavior; 2) wet dog shake; 3) face twitch; 4) clonus or head jerking; and 5) running and jumping.

In addition to these video-EEG experiments, a series of EEG-paired stimulations were performed under the same conditions as fMRI experiments with light anesthesia and ventilation (n = 2 DH-injected; n = 3 IH-injected) to determine if the EEG responses evoked in awake animals could also be evoked under anesthesia during fMRI. Screw electrodes were implanted above the hippocampus as described above, and animals were allowed to recover for at least a week before proceeding. Matching the ofMRI experiments, animals were artificially ventilated (45–55 strokes/min) under light anesthesia using a ventilator and calibrated vaporizer with a mixture of O_2 (35%), N_2O (63.5%), and isoflurane (1.2–1.5%). Expiratory CO_2 was kept at 3–4%, and body temperature was maintained at 36–38 °C using an electronically controlled heating pad (FHC Inc.). Stimulation was delivered with the same 20 s on / 40 s off six-cycle paradigm used for imaging.

To compare the seizure-like EEG responses observed under anesthesia with an established model of acute seizures, we also collected EEG recordings in awake (n = 2) and anesthetized (n = 3) naïve animals injected with pilocarpine (Sigma-Aldrich). Screw electrodes were implanted above the hippocampus as described above, and animals were allowed to recover for at least a week before proceeding with experiments. We first determined the dose to induce status epilepticus in awake rats, after which we attempted to induce seizures under the anesthetic conditions used for ofMRI imaging and EEG-paired, anesthetized stimulations described above. Awake rats were injected i.p. with 320 mg/kg of pilocarpine, and additional doses were given every 60 min until the emergence of status epilepticus, which was assessed using EEG and behavior (Racine stage 3+). Due to the seizure suppressing effect of isoflurane, anesthetized rats were administered a higher initial dose of pilocarpine at 480 mg/kg, followed by 320 mg/kg every 30 min during which EEG was continuously recorded to assess the emergence of seizures. Rats were administered methylscopolamine (Sigma-Aldrich) 30 min prior to pilocarpine to reduce peripheral cholinergic effects.

2.6 Histology

Upon completion of all *in vivo* studies, a cohort of the imaged rats (n = 2 DH-injected; n = 2 IH-injected) was deeply anesthetized with isoflurane in a knockdown box and transcardially perfused with 0.1M PBS and ice-cold 4% paraformaldehyde (PFA) in PBS. Brains were extracted and fixed in 4% PFA overnight at 4 °C. The brains were equilibrated in 10%, 20% and then 30% sucrose in PBS at 4 °C. Coronal sections (50 μm) were prepared on a freezing microtome (HM 430 Sliding Microtome, Thermo Scientific Inc.). Consecutive sections (500 μm apart) were mounted and examined with a fluorescent microscope (Leica EL6000).

For immunohistochemistry, free-floating sections were processed with 2% normal donkey serum, 1% bovine serum albumin, and 0.2% Triton X-100 for 30 minutes. Sections were then exposed at 4 °C for 48 hours to primary antibodies against mouse monoclonal CaMKIIα (1:400, Abcam) and rabbit polyclonal gamma amino-butyric acid (GABA; 1:10K, Calbiochem). After washing with PBS, sections were then incubated for 2 hours at room

temperature with secondary antibodies Alexa Fluor®594-conjugated AffiniPure donkey anti-mouse IgG and Alexa Fluor®647-conjugated AffiniPure donkey anti-rabbit IgG (both 1:1000, Jackson Laboratories). Slices were then washed, incubated with DAPI (1:50,000) for 20 min, washed again, and mounted on slides with PVA-Dabco (Sigma-Aldrich). Double or triple immuno-fluorescence was assessed with a laser confocal microscope (Leica CTR 6500).

3. Results

3.1 ofMRI of Hippocampal Stimulation

Virally mediated optogenetic techniques were used in these experiments to achieve selective stimulation of excitatory (CaMKIIa-expressing) pyramidal neurons of the dorsal (DH) or intermediate (IH) hippocampus. T2-weighted anatomical MRI scans confirmed the proper location of optical fibers in all animals used for fMRI scanning (Fig. 1A,C). Histological examination also confirmed that ChR2-EYFP was localized to CaMKIIa-positive cells of the targeted hippocampal region, and not to GABAergic inhibitory cells (Fig. 1B,D–F). For animals injected in dorsal hippocampus, EYFP-expressing axonal projections were observed in the medial septal nuclei, retrosplenial cortex, dorsal thalamus, and both ipsilateral and contralateral subiculum (Fig. S2A). On the other hand, for animals injected in intermediate hippocampus, EYFP-expressing axonal projections were observed in the lateral septal nuclei, nucleus accumbens, fimbria, dorsal thalamus, and parts of the dorsal hippocampus (CA2/CA3) (Fig. S2B). Cortical regions with EYFP expression included the medial prefrontal, retrosplenial, adjacent sensory/auditory/parietal cortices, and to a lesser extent the parahippocampal region. Compared to DH injections, significantly less expression was observed in the contralateral hippocampus.

To determine how these anatomical connections give rise to dynamic network activity driven by dorsal and intermediate hippocampus stimulations, whole brain functional imaging data was collected with high temporal resolution using a 750 ms moving window reconstruction algorithm (Fang and Lee, 2013). 23 coronal slices with 0.5×0.5 mm^2 in-plane spatial resolution and 0.5 mm slice thickness were acquired during DH (Fig. 2A) or IH (Fig. 2C) stimulation at frequencies ranging from 6 to 60 Hz. High SNR was achieved across the brain, with minimal susceptibility artifacts from implanted fibers (Fig. S3A,B). Robust activation was observed at the site of stimulation across frequencies for both locations of stimulation (Fig. 2E,F). Time series of active voxels at the site of stimulation exhibited strong positive responses across frequencies (Fig. 2B,D). In contrast, light delivery failed to elicit any responses in control animals without ChR2 expression, confirming that the observed BOLD effects were a result of direct ChR2 stimulation and not heating related artifact (Christie et al., 2012) (Fig. S3C,D).

Visualization of active voxels in the averaged group analysis images revealed the specific networks recruited with each set of stimulation parameters. For example, during 40 Hz DH stimulation, BOLD activity was mostly restricted to the dorsal hippocampus and subiculum, with some activation in the retrosplenial cortex (Fig. 2G, Video S1). On the other hand, stimulation of IH at the same frequency activated both dorsal and intermediate portions of hippocampus, cortex (sensory, insular, cingulate, retrosplenial, visual, and auditory), septal

nuclei, and hypothalamus (Fig. 2H, Video S2). Lower frequency stimulation at 6 Hz resulted in limited activity in areas other than the proximal region of stimulation for both DH and IH experiments (Fig. S4). These frequency-dependent effects were not due to any other differences in protocol, since the same animals were used across frequencies, other parameters of stimulation such as laser power and duty cycle were identical, and the order of stimulation frequency was randomized.

3.2 Spatial Patterns of Network Recruitment

To quantify the extent and pattern of activation across the brain, we first delineated various ROIs encompassing the hippocampus, recruited subcortical areas (i.e. septal nuclei and hypothalamus), and limbic cortex (cingulate, insular, and retrosplenial) (Fig. 3A). After grouping active voxels into their respective ROIs, we calculated the total activation volume for each region across individual animals and for each experimental group's average image. The combined subcortical ROI was found to have a statistically significant difference in activation volume between DH and IH stimulations, with IH stimulation recruiting greater volume at 6, 10, 20, and 40 Hz (Fig. 3C). Similarly, IH stimulations at 10, 20, and 40 Hz recruited greater volumes of cingulate cortex than DH stimulations (Fig. 3D), and IH stimulations at 20 and 40 Hz recruited greater volumes of insular cortex than DH stimulations (Fig. 3E). Indeed, across frequencies, DH stimulation achieved minimal activation of these cortical areas. In contrast, recruitment of retrosplenial cortex was common to both stimulation locations, with recruitment during DH stimulation even surpassing that of IH stimulation at 60 Hz (Fig. 3F). Despite these differences in the extended network, the total volume of activation in the hippocampus was not significantly different between DH and IH stimulations (Fig. 3B). This suggests that the spread of activity from the hippocampus to other subcortical and cortical structures was the result of engaging specific hippocampal circuits, rather than achieving a certain amount of hippocampal activation. Note that while not all stimulation frequencies were collected with the same number of animals, a sufficient number was collected to identify statistical differences between DH and IH stimulations for all frequencies.

3.3 Temporal Dynamics of Global Activity

In addition to a spatial characterization of global recruitment patterns, ofMRI enables the whole-brain temporal dynamics of optogenetically evoked responses to be observed and quantified. Temporal analysis of the responses evoked during DH and IH stimulations revealed that functionally distinct networks were engaged during stimulation of either region. For example, during 40 Hz DH and IH stimulations, the response at the ipsilateral hippocampus increased at a faster rate than the contralateral side's response (Fig. 4A). Among active subcortical structures during IH stimulation, the septal nuclei had a more prolonged response than hypothalamus (Fig. 4B). Interestingly, the insular, cingulate, and retrosplenial cortical regions all showed similar dynamics with a short positive response and fast decay rate (Fig. 4C). The insular cortex also exhibited a significant post-stimulus undershoot. To quantify the differences in temporal dynamics amongst these regions, we performed a voxelwise cross-correlation analysis. The resulting correlation matrices show that during DH stimulation, most of the active voxels belong to the hippocampus and share similar dynamics (mean cross-correlation coefficient $r = 0.85 \pm 0.13$ STD) (Fig. 4D). The

active cortical voxels, however, exhibit reduced correlation with the hippocampus (r = 0.49 ± 0.22 STD), indicating the distinct temporal evolution of this region's response. Similarly, the much larger multi-region cortical network engaged during IH stimulation also has reduced correlation with the recruited hippocampus and subcortical voxels (r = 0.49 ± 0.18 STD), further illustrating the distinct dynamics observed in active circuits (Fig. 4E).

An interesting finding from the global temporal analysis was that the contralateral dentate gyrus exhibited a distinctly negative BOLD response during DH stimulation. This response was present at all frequencies above 6 Hz for DH stimulations (Fig. 5A). Activation maps confirm the specific localization of this response to the dentate gyrus within the hippocampus (Fig. 5B,C). Interestingly, this negative response was absent from IH stimulations, which led to positive BOLD signals throughout the hippocampus (Fig. 5D). Quantification of this effect showed a statistically significant difference in dentate gyrus volume with negative BOLD signal between DH and IH stimulations at 20, 40, and 60 Hz (Fig. 5E). This trend was also observed in the group averages (Fig. 5F).

3.4 EEG and behavioral correlates of ofMRI

In analyzing the temporal dynamics of evoked responses, we found that higher frequencies of stimulation resulted in sustained HRFs in the hippocampus. This trend is exemplified by the HRFs for 6 and 60 Hz, the lowest and highest frequencies that we tested, shown in Figure 6A. Comparison with another region's HRFs in Figure 6B shows that this trend over frequency was not generalizable across all brain areas. Quantification of the HRF duration, defined as the amount of time for which the HRF stayed above 40% its maximum value, confirmed this frequency-dependent increase in response length. For both DH and IH experiments, stimulation at 20, 40, and 60 Hz resulted in average hippocampal HRFs with a duration significantly greater than those of the corresponding 6 Hz case (Fig. 6C). Across all active hippocampal voxels, the distribution of durations also increased with frequency (Fig. 6D).

Because the dynamics of ofMRI HRFs have been shown to reflect the timing of underlying neuronal activity (Kahn et al., 2011; Lee et al., 2010), we hypothesized that these sustained responses could reflect seizure-like afterdischarge activities within the hippocampus. To investigate this relationship, EEG-paired stimulations were delivered in lightly anesthetized (1.2–1.5% isoflurane) and ventilated animals using the same stimulation paradigm as ofMRI. Importantly, this level of anesthesia (the same used for ofMRI) was sufficiently low to obtain stable EEG recordings and observe evoked responses (Fig. S5A). Furthermore, high frequency stimulations under this anesthetized condition could repeatedly evoke seizure-like afterdischarges in all dorsal and intermediate hippocampus-stimulated animals tested (Table S1, Fig. S5). This is unlike other acute seizure models, such as the kainic acid (Airaksinen et al., 2010), bupivacaine (Fukuda et al., 1996), and pilocarpine (Fig. S6) models, for which isoflurane anesthesia attenuates or completely abolishes seizures.

To characterize the specific phenotype of these optogenetically-evoked seizures, subdural EEG recordings and video surveillance were also collected during repeated DH or IH stimulations in awake, behaving animals. Evolving EEG seizure activity was observed during both DH and IH stimulations at frequencies above 10 Hz (Fig. 6E.*i*,F,G, Videos S3

and S4). Across animals, the average afterdischarge length of evoked seizures was 25.8 ± 2.9 s (SEM, $n = 7$). In addition to electrographic responses, seizure-like behavior of face twitching and wet dog shakes were observed for both stimulation locations, but were more pronounced and consistent across frequencies for IH stimulation (Fig. 6E.*ii*). More severe behavior indicative of generalized seizures, including clonus and wild running and jumping, was also observed, but only during IH stimulations (Fig. 6E.*iii*, Videos S3 and S4). DH stimulation therefore evoked electrographic seizures, whereas IH stimulation evoked generalized electrographic and behavioral seizures. Combining this result with those of the ofMRI experiments, we conclude that ofMRI-visualized activity provided prediction on the type of evoked seizures. For stimulations that resulted in mostly local activations, the electrographic responses were not accompanied by behavioral seizures. However, for stimulations that led to widespread network recruitment including cortical areas, the evoked seizures generalized and led to stereotyped seizure behavior.

4. Discussion

Using the novel imaging modality of optogenetic fMRI, this study shows that cell type-specific stimulations of dorsal and intermediate hippocampus each give rise to functionally distinct global network activities with region-specific temporal dynamics. The recruitment of these networks was dependent on the precise frequency of stimulation, demonstrating the importance of temporal encoding in fully characterizing a circuit's function and behavior (Lee, 2011). Pointing to the predictive power of these dynamics, we also found that sustained hemodynamic responses observed during high frequency stimulation were correlated with ictal afterdischarges in separate anesthetized and awake EEG experiments, and that large-scale networks recruited during IH stimulation were correlated with clonic behavioral seizures. Collectively, these results provide insight into the functional role of hippocampal circuitry and show that ofMRI can identify large-scale networks in the brain that correlate with specific behavioral and electrophysiological markers.

The distinct anatomical projections originating from the dorsal and intermediate hippocampus reported here (Fig. S2) provide context for the observed BOLD signals and are consistent with previous findings. For example, tracer studies have shown that dorsal CA1 projects to the medial septal nuclei, retrosplenial cortex, and bilateral subiculum, while more ventral parts of CA1 project to the lateral septal nuclei, nucleus accumbens, fimbria, and medial prefrontal and parahippocampal (e.g. entorhinal) cortex (Cenquizca and Swanson, 2007; Gabbott et al., 2002; Swanson, 1981; van Groen and Wyss, 1990). CA1 projections to thalamus have also been reported (Cenquizca and Swanson, 2006). While strong projections from the far ventral pole of CA1 to hypothalamus have been reported (Cenquizca and Swanson, 2006, 2007; Chiba, 2000), we did not identify projections in this region from either dorsal or intermediate hippocampus.

Importantly, the functional activities observed in our ofMRI experiments inform the significance of these underlying anatomical connections by revealing which direct connections are engaged, as well as which regions that are not directly connected become active. For example, robust activity was observed at high frequencies of DH stimulation in the anatomically connected subiculum and retrosplenial cortex, but not in the septal nuclei,

another major target of anatomical projections. On the other hand, robust activity during IH stimulation was observed in remote targets of the stimulated population (e.g. septal nuclei and retrosplenial cortex), as well as in regions not receiving significant projections such as the contralateral hippocampus and insular cortex (Jay et al., 1989). These findings are consistent with previous reports of functional connectivity between the hippocampus and both cortical and subcortical limbic structures (Englot et al., 2008; Helbing et al., 2013; Ranganath et al., 2005). While other functional imaging studies using direct stimulation of the hippocampus have not reported widespread recruitment beyond the hippocampal formation (Abe et al., 2012; Angenstein et al., 2007; Canals et al., 2009), these studies also offer important additional insight into which hippocampal dynamics affect global brain circuitry. Such differences in evoked responses may be due to the specific stimulation parameters employed, image acquisition methods, or the particular subregion of the hippocampal formation targeted for stimulation. In particular, the application of optogenetic, rather than electrical, stimulation with ofMRI may lead to previously unobserved responses, since it targets stimulation to a specific genetically and anatomically defined population.

As a relatively new technology, ofMRI is expected to provide a powerful tool for dissecting the neuronal function of global brain circuits. However, its ability to visualize diverse dynamics throughout the brain has not yet been demonstrated. Here, we report specific examples of how this new tool (ofMRI) enables direct measurement of detailed network dynamics. First, we find that targeted stimulation of a genetically defined population within a relatively confined anatomical location can lead to robust activation throughout the brain. While prior ofMRI experiments have independently evoked activation in different areas of the brain, including cortex (Desai et al., 2011), hippocampus (Abe et al., 2012), and midbrain (Domingos et al., 2011), such widespread activity has not yet been reported from a single stimulus. Indeed, the widespread brain activation evoked by IH stimulation is expected to reflect a polysynaptic response in regions such as the contralateral hippocampus, hypothalamus, and insular and cingulate cortex. To the best of our knowledge, this is the first report of ofMRI detecting such activities.

Our study also demonstrates that ofMRI can be used to non-invasively study how the temporal dynamics of stimulations affect the brain’s response. Studying the downstream response in this way is important for three reasons. First, although a region may exhibit certain projections, connections alone do not guarantee a functional engagement. Second, even if two regions do not exhibit direct uni- or bi-directional projections to one another, there may still be a causal link between them. Third, the temporal evolution of a projection’s activity likely plays an important role in how the neuronal firing ultimately translates to higher-level phenomena such as cognition and behavior. The dynamic nature of neuronal circuit function was exemplified in our study by the observed dependence of activation extent, HRF duration, and HRF polarity on the frequency of stimulation (Fig. 3 and Fig. 6A–D).

In the context of functional neuroanatomy, we have shown that exciting a single population of genetically and anatomically defined neurons along the dorsoventral axis of the hippocampus at specific frequencies can generate seizures with distinct behavioral and physiological manifestations. While seizure generation using optogenetic stimulation of the

hippocampus has previously been reported (Osawa et al., 2013), our study is the first to generate seizures through stimulation of a CaMKIIa-positive subset of neurons, and the first to demonstrate behavioral as well as electrographic seizures. Importantly, our study also demonstrates the dependence of seizure characteristics on small changes in both the location and temporal pattern of stimulation. These results suggest that novel seizure models can be developed by optogenetically stimulating specific neuronal populations and evoking seizures of precise origin, while the dynamics of their network engagements can be visualized using ofMRI. For example, given our observation of optogenetically evoked evolving seizures and seizure-like afterdischarges under anesthesia (Table S1, Fig. S5), the extended recruitment of cortical and subcortical structures visualized during IH stimulation likely not only predicts the presence of behavioral seizures, but also reflects the specific network engagement underlying that response. This finding highlights an important advantage of the optogenetic method used here, since it enables classical, evolving seizures to be evoked under anesthesia and therefore imaged *in vivo*. Future studies utilizing this approach could lead to a better understanding of the seizure networks that underlie specific phenotypes of epilepsy (Airaksinen et al., 2010; Tenney et al., 2003). A better understanding of pathway-specific seizure networks could in turn facilitate the targeting of focal seizure therapies, such as lesions, drug infusions, or neurostimulation.

Finally, the observed association between distinct hippocampal recruitment patterns and different seizure phenotypes may provide an explanation for the heterogeneity of seizure types seen in patients who exhibit diverse patterns of hippocampal pathology (Forsgren et al., 1996; Thom et al., 2012). For example, we found that a strong negative BOLD response was evoked in the contralateral dentate gyrus during high frequency DH, but not IH, stimulation. Since DH stimulation did not result in widespread brain recruitment or generalized seizures, this negative BOLD signal in dentate gyrus could be related to a mechanism that governs seizure propagation beyond the hippocampus. The exact source of the negative BOLD signal requires further investigation (Devor et al., 2007; Harel et al., 2002; Kim and Ogawa, 2012; Schulz et al., 2012). However, it has been proposed that decreases in lateral inhibition of the dentate gyrus decrease seizure threshold (Sloviter, 1987, 1991, 1994). Our results support this view, since the observed signal could represent an increase in lateral inhibition (Hamzei et al., 2002; Northoff et al., 2007) that increases seizure threshold and consequently prevents hippocampal seizures from generalizing to other regions.

5. Conclusion

In summary, we have demonstrated the first use of ofMRI to investigate the global, frequency-dependent network activities of cell type-specific neuronal populations within two hippocampal subregions. We show that stimulations of intermediate hippocampus at high frequencies recruit widespread cortical and subcortical networks, while stimulations of dorsal hippocampus result in activity primarily restricted to the stimulation site. A negative BOLD signal in contralateral dentate gyrus observed with DH stimulation may underlie a possible mechanism for these differences. Importantly, separate stimulation of these two regions during video-EEG experiments were shown to evoke distinct seizure phenotypes,

suggesting that ofMRI can be used to study the large-scale functional networks associated with a diverse range of behavior.

Supplementary Material

Refer to Web version on PubMed Central for supplementary material.

Acknowledgements

This work was supported by the NIH/NIBIB R00 Award (4R00EB008738), Okawa Foundation Research Grant Award, NIH Director's New Innovator Award (1DP2OD007265), the NSF CAREER Award (1056008), and the Alfred P. Sloan Research Fellowship. R.S.F. was supported by the James and Carrie Anderson Fund for Epilepsy Research, and the Susan Horngren and Littlefield Funds. A.J.W was supported by a Bio-X Bioengineering Graduate Fellowship. J.H.L. would like to acknowledge Karl Deisseroth for providing the DNA plasmids and for helpful suggestions, and Josef Parvizi for his contribution to the interpretation of preliminary results and the planning of the study's later stages. The authors thank the Lee Lab members for their contribution to ofMRI experiments. The authors would also like to thank Mason Porter, Michael Lin, and Aaron Gitler for critically reading the manuscript and for helpful suggestions.

Abbreviations

DH dorsal hippocampus

IH intermediate hippocampus

References

Abe Y, Sekino M, Terazono Y, Ohsaki H, Fukazawa Y, Sakai S, Yawo H, Hisatsune T. Opto-fMRI analysis for exploring the neuronal connectivity of the hippocampal formation in rats. Neurosci Res. 2012; 74:248–255. [PubMed: 22982343]

Adamantidis AR, Zhang F, Aravanis AM, Deisseroth K, de Lecea L. Neural substrates of awakening probed with optogenetic control of hypocretin neurons. Nature. 2007; 450:420–424. [PubMed: 17943086]

Airaksinen AM, Niskanen JP, Chamberlain R, Huttunen JK, Nissinen J, Garwood M, Pitkanen A, Grohn O. Simultaneous fMRI and local field potential measurements during epileptic seizures in medetomidine-sedated rats using raser pulse sequence. Magn Reson Med. 2010; 64:1191–1199. [PubMed: 20725933]

Angenstein F, Kammerer E, Niessen HG, Frey JU, Scheich H, Frey S. Frequency-dependent activation pattern in the rat hippocampus, a simultaneous electrophysiological and fMRI study. Neuroimage. 2007; 38:150–163. [PubMed: 17728153]

Aravanis AM, Wang LP, Zhang F, Meltzer LA, Mogri MZ, Schneider MB, Deisseroth K. An optical neural interface: in vivo control of rodent motor cortex with integrated fiberoptic and optogenetic technology. J Neural Eng. 2007; 4:S143–S156. [PubMed: 17873414]

Ashton D, Van Reempts J, Haseldonckx M, Willems R. Dorsal-ventral gradient in vulnerability of CA1 hippocampus to ischemia: a combined histological and electrophysiological study. Brain Res. 1989; 487:368–372. [PubMed: 2731049]

Bandettini PA, Jesmanowicz A, Wong EC, Hyde JS. Processing strategies for time-course data sets in functional MRI of the human brain. Magn Reson Med. 1993; 30:161–173. [PubMed: 8366797]

Boyden ES, Zhang F, Bamberg E, Nagel G, Deisseroth K. Millisecond-timescale, genetically targeted optical control of neural activity. Nat Neurosci. 2005; 8:1263–1268. [PubMed: 16116447]

Bullmore E, Sporns O. Complex brain networks: graph theoretical analysis of structural and functional systems. Nat Rev Neurosci. 2009; 10:186–198. [PubMed: 19190637]

Canals S, Beyerlein M, Merkle H, Logothetis NK. Functional MRI evidence for LTP-induced neural network reorganization. Curr Biol. 2009; 19:398–403. [PubMed: 19230667]

Canals S, Beyerlein M, Murayama Y, Logothetis NK. Electric stimulation fMRI of the perforant pathway to the rat hippocampus. Magn Reson Imaging. 2008; 26:978–986. [PubMed: 18479870]

Carter ME, Yizhar O, Chikahisa S, Nguyen H, Adamantidis A, Nishino S, Deisseroth K, de Lecea L. Tuning arousal with optogenetic modulation of locus coeruleus neurons. Nat Neurosci. 2010; 13:1526–1533. [PubMed: 21037585]

Cenquizca LA, Swanson LW. Analysis of direct hippocampal cortical field CA1 axonal projections to diencephalon in the rat. J Comp Neurol. 2006; 497:101–114. [PubMed: 16680763]

Cenquizca LA, Swanson LW. Spatial organization of direct hippocampal field CA1 axonal projections to the rest of the cerebral cortex. Brain Res Rev. 2007; 56:1–26. [PubMed: 17559940]

Chiba T. Collateral projection from the amygdalo--hippocampal transition area and CA1 to the hypothalamus and medial prefrontal cortex in the rat. Neurosci Res. 2000; 38:373–383. [PubMed: 11164564]

Christie IN, Wells JA, Southern P, Marina N, Kasparov S, Gourine AV, Lythgoe MF. fMRI response to blue light delivery in the naive brain: Implications for combined optogenetic fMRI studies. Neuroimage. 2012; 66C:634–641. [PubMed: 23128081]

de No RL. Studies on the structure of the cerebral cortex XI Continuation of the study of the ammonic system. Journal Fur Psychologie Und Neurologie. 1934; 46:113–177.

Desai M, Kahn I, Knoblich U, Bernstein J, Atallah H, Yang A, Kopell N, Buckner RL, Graybiel AM, Moore CI, Boyden ES. Mapping brain networks in awake mice using combined optical neural control and fMRI. J Neurophysiol. 2011; 105:1393–1405. [PubMed: 21160013]

Devor A, Tian P, Nishimura N, Teng IC, Hillman EM, Narayanan SN, Ulbert I, Boas DA, Kleinfeld D, Dale AM. Suppressed neuronal activity and concurrent arteriolar vasoconstriction may explain negative blood oxygenation level-dependent signal. J Neurosci. 2007; 27:4452–4459. [PubMed: 17442830]

Domingos AI, Vaynshteyn J, Voss HU, Ren X, Gradinaru V, Zang F, Deisseroth K, de Araujo IE, Friedman J. Leptin regulates the reward value of nutrient. Nat Neurosci. 2011; 14:1562–1568. [PubMed: 22081158]

Dong HW, Swanson LW, Chen L, Fanselow MS, Toga AW. Genomic-anatomic evidence for distinct functional domains in hippocampal field CA1. Proc Natl Acad Sci U S A. 2009; 106:11794–11799. [PubMed: 19561297]

Engel SA, Glover GH, Wandell BA. Retinotopic organization in human visual cortex and the spatial precision of functional MRI. Cereb Cortex. 1997; 7:181–192. [PubMed: 9087826]

Englot DJ, Mishra AM, Mansuripur PK, Herman P, Hyder F, Blumenfeld H. Remote effects of focal hippocampal seizures on the rat neocortex. J Neurosci. 2008; 28:9066–9081. [PubMed: 18768701]

Fang Z, Lee JH. High-throughput optogenetic functional magnetic resonance imaging with parallel computations. J Neurosci Methods. 2013; 218:184–195. [PubMed: 23747482]

Fanselow MS, Dong HW. Are the dorsal and ventral hippocampus functionally distinct structures? Neuron. 2010; 65:7–19. [PubMed: 20152109]

Forsgren L, Bucht G, Eriksson S, Bergmark L. Incidence and clinical characterization of unprovoked seizures in adults: a prospective population-based study. Epilepsia. 1996; 37:224–229. [PubMed: 8598179]

Fukuda H, Hirabayashi Y, Shimizu R, Saitoh K, Mitsuhata H. Sevoflurane is equivalent to isoflurane for attenuating bupivacaine-induced arrhythmias and seizures in rats. Anesth Analg. 1996; 83:570–573. [PubMed: 8780283]

Gabbott P, Headlam A, Busby S. Morphological evidence that CA1 hippocampal afferents monosynaptically innervate PV-containing neurons and NADPH-diaphorase reactive cells in the medial prefrontal cortex (Areas 25/32) of the rat. Brain Res. 2002; 946:314–322. [PubMed: 12137936]

Garcia Ruiz AJ, Zambelli M, La Porta C, Ladinsky H, Consolo S. Differences between rat dorsal and ventral hippocampus in muscarinic receptor agonist binding and interaction with phospholipase C. Eur J Pharmacol. 1993; 244:125–131. [PubMed: 8432309]

Gilbert M, Racine RJ, Smith GK. Epileptiform burst responses in ventral vs dorsal hippocampal slices. Brain Res. 1985; 361:389–391. [PubMed: 4084805]

Glover GH, Lee AT. Motion artifacts in fMRI: comparison of 2DFT with PR and spiral scan methods. Magn Reson Med. 1995; 33:624–635. [PubMed: 7596266]

Goloshevsky AG, Silva AC, Dodd SJ, Koretsky AP. BOLD fMRI and somatosensory evoked potentials are well correlated over a broad range of frequency content of somatosensory stimulation of the rat forepaw. Brain Res. 2008; 1195:67–76. [PubMed: 18206862]

Gradinaru V, Mogri M, Thompson KR, Henderson JM, Deisseroth K. Optical deconstruction of parkinsonian neural circuitry. Science. 2009; 324:354–359. [PubMed: 19299587]

Hamzei F, Dettmers C, Rzanny R, Liepert J, Buchel C, Weiller C. Reduction of excitability ("inhibition") in the ipsilateral primary motor cortex is mirrored by fMRI signal decreases. Neuroimage. 2002; 17:490–496. [PubMed: 12482101]

Harel N, Lee SP, Nagaoka T, Kim DS, Kim SG. Origin of negative blood oxygenation level-dependent fMRI signals. J Cereb Blood Flow Metab. 2002; 22:908–917. [PubMed: 12172376]

Helbing C, Werner G, Angenstein F. Variations in the temporal pattern of perforant pathway stimulation control the activity in the mesolimbic pathway. Neuroimage. 2013; 64:43–60. [PubMed: 22982727]

Henkelman RM. Measurement of signal intensities in the presence of noise in MR images. Med Phys. 1985; 12:232–233. [PubMed: 4000083]

Hock BJ Jr, Bunsey MD. Differential effects of dorsal and ventral hippocampal lesions. J Neurosci. 1998; 18:7027–7032. [PubMed: 9712671]

Huettel, SA.; Song, AW.; McCarthy, G. Functional magnetic resonance imaging. Sunderland, MA: Sinauer Associates; 2004.

Jackson JI, Meyer CH, Nishimura DG, Macovski A. Selection of a convolution function for Fourier inversion using gridding [computerised tomography application]. IEEE Trans Med Imaging. 1991; 10:473–478. [PubMed: 18222850]

Jay TM, Glowinski J, Thierry AM. Selectivity of the hippocampal projection to the prelimbic area of the prefrontal cortex in the rat. Brain Res. 1989; 505:337–340. [PubMed: 2598054]

Jung MW, Wiener SI, McNaughton BL. Comparison of spatial firing characteristics of units in dorsal and ventral hippocampus of the rat. J Neurosci. 1994; 14:7347–7356. [PubMed: 7996180]

Kahn I, Desai M, Knoblich U, Bernstein J, Henninger M, Graybiel AM, Boyden ES, Buckner RL, Moore CI. Characterization of the functional MRI response temporal linearity via optical control of neocortical pyramidal neurons. J Neurosci. 2011; 31:15086–15091. [PubMed: 22016542]

Kim DH, Adalsteinsson E, Spielman DM. Simple analytic variable density spiral design. Magn Reson Med. 2003; 50:214–219. [PubMed: 12815699]

Kim DS, Ronen I, Olman C, Kim SG, Ugurbil K, Toth LJ. Spatial relationship between neuronal activity and BOLD functional MRI. Neuroimage. 2004; 21:876–885. [PubMed: 15006654]

Kim SG, Ogawa S. Biophysical and physiological origins of blood oxygenation level-dependent fMRI signals. J Cereb Blood Flow Metab. 2012; 32:1188–1206. [PubMed: 22395207]

Lee JH. Tracing activity across the whole brain neural network with optogenetic functional magnetic resonance imaging. Front Neuroinform. 2011; 5:21. [PubMed: 22046160]

Lee JH. Informing brain connectivity with optogenetic functional magnetic resonance imaging. Neuroimage. 2012; 62:2244–2249. [PubMed: 22326987]

Lee JH, Durand R, Gradinaru V, Zhang F, Goshen I, Kim DS, Fenno LE, Ramakrishnan C, Deisseroth K. Global and local fMRI signals driven by neurons defined optogenetically by type and wiring. Nature. 2010; 465:788–792. [PubMed: 20473285]

Mattis J, Tye KM, Ferenczi EA, Ramakrishnan C, O'Shea DJ, Prakash R, Gunaydin LA, Hyun M, Fenno LE, Gradinaru V, Yizhar O, Deisseroth K. Principles for applying optogenetic tools derived from direct comparative analysis of microbial opsins. Nat Methods. 2012; 9:159–172. [PubMed: 22179551]

Northoff G, Walter M, Schulte RF, Beck J, Dydak U, Henning A, Boeker H, Grimm S, Boesiger P. GABA concentrations in the human anterior cingulate cortex predict negative BOLD responses in fMRI. Nat Neurosci. 2007; 10:1515–1517. [PubMed: 17982452]

Osawa S, Iwasaki M, Hosaka R, Matsuzaka Y, Tomita H, Ishizuka T, Sugano E, Okumura E, Yawo H, Nakasato N, Tominaga T, Mushiake H. Optogenetically induced seizure and the longitudinal hippocampal network dynamics. PLoS One. 2013; 8:e60928. [PubMed: 23593349]

Paxinos, G.; Watson, C. The rat brain in stereotaxic coordinates: hard cover edition. Academic press; 2006.

Ranganath C, Heller A, Cohen MX, Brozinsky CJ, Rissman J. Functional connectivity with the hippocampus during successful memory formation. Hippocampus. 2005; 15:997–1005. [PubMed: 16281291]

Rivard AL, Simura KJ, Mohammed S, Magembe AJ, Pearson HM, Hallman MR, Barnett SJ, Gatlin DL, Gallegos RP, Bianco RW. Rat intubation and ventilation for surgical research. Journal of Investigative Surgery. 2006; 19:267–274. [PubMed: 16835141]

Schulz K, Sydekum E, Krueppel R, Engelbrecht CJ, Schlegel F, Schroter A, Rudin M, Helmchen F. Simultaneous BOLD fMRI and fiber-optic calcium recording in rat neocortex. Nat Methods. 2012; 9:597–602. [PubMed: 22561989]

Siegel A, Flynn JP. Differential effects of electrical stimulation and lesions of the hippocampus and adjacent regions upon attack behavior in cats. Brain Res. 1968; 7:252–267. [PubMed: 5689034]

Sijbers J, Den Dekker A, Van Dyck D, Raman E. Estimation of signal and noise from Rician distributed data. Proceedings of the International Conference on Signal Processing and Communications. 1998:140–142.

Sloviter RS. Decreased hippocampal inhibition and a selective loss of interneurons in experimental epilepsy. Science. 1987; 235:73–76. [PubMed: 2879352]

Sloviter RS. Permanently altered hippocampal structure, excitability, and inhibition after experimental status epilepticus in the rat: the "dormant basket cell" hypothesis and its possible relevance to temporal lobe epilepsy. Hippocampus. 1991; 1:41–66. [PubMed: 1688284]

Sloviter RS. The functional organization of the hippocampal dentate gyrus and its relevance to the pathogenesis of temporal lobe epilepsy. Ann Neurol. 1994; 35:640–654. [PubMed: 8210220]

Swanson LW. A direct projection from Ammon's horn to prefrontal cortex in the rat. Brain Res. 1981; 217:150–154. [PubMed: 7260612]

Tanaka KF, Samuels BA, Hen R. Serotonin receptor expression along the dorsal-ventral axis of mouse hippocampus. Philos Trans R Soc Lond B Biol Sci. 2012; 367:2395–2401. [PubMed: 22826340]

Tenney JR, Duong TQ, King JA, Ludwig R, Ferris CF. Corticothalamic modulation during absence seizures in rats: a functional MRI assessment. Epilepsia. 2003; 44:1133–1140. [PubMed: 12919383]

Thom M, Liagkouras I, Martinian L, Liu J, Catarino CB, Sisodiya SM. Variability of sclerosis along the longitudinal hippocampal axis in epilepsy: a post mortem study. Epilepsy Res. 2012; 102:45–59. [PubMed: 22608064]

Van Groen T, Lopes da Silva FH. Septotemporal distribution of entorhinal projections to the hippocampus in the cat: electrophysiological evidence. J Comp Neurol. 1985; 238:1–9. [PubMed: 4044899]

van Groen T, Wyss JM. Extrinsic projections from area CA1 of the rat hippocampus: olfactory, cortical, subcortical, and bilateral hippocampal formation projections. J Comp Neurol. 1990; 302:515–528. [PubMed: 1702115]

Vazquez AL, Fukuda M, Crowley JC, Kim SG. Neural and Hemodynamic Responses Elicited by Forelimb- and Photo-stimulation in Channelrhodopsin-2 Mice: Insights into the Hemodynamic Point Spread Function. Cereb Cortex. 2013

Weitz AJ, Lee JH. Progress with optogenetic functional MRI and its translational implications. Future Neurology. 2013; 8:691–700.

Yizhar O, Fenno LE, Davidson TJ, Mogri M, Deisseroth K. Optogenetics in neural systems. Neuron. 2011; 71:9–34. [PubMed: 21745635]

Yu X, Wang S, Chen DY, Dodd S, Goloshevsky A, Koretsky AP. 3D mapping of somatotopic reorganization with small animal functional MRI. Neuroimage. 2010; 49:1667–1676. [PubMed: 19770051]

Zhao S, Ting JT, Atallah HE, Qiu L, Tan J, Gloss B, Augustine GJ, Deisseroth K, Luo M, Graybiel AM, Feng G. Cell type-specific channelrhodopsin-2 transgenic mice for optogenetic dissection of neural circuitry function. Nat Methods. 2011; 8:745–752. [PubMed: 21985008]

Highlights

- Stimulation of intermediate, but not dorsal, hippocampus evokes widespread activity
- Dynamic network engagement varies with stimulation frequency
- Stimulation of dorsal hippocampus evokes negative BOLD signal in dentate gyrus
- ofMRI responses predict electrographic and behavioral seizures

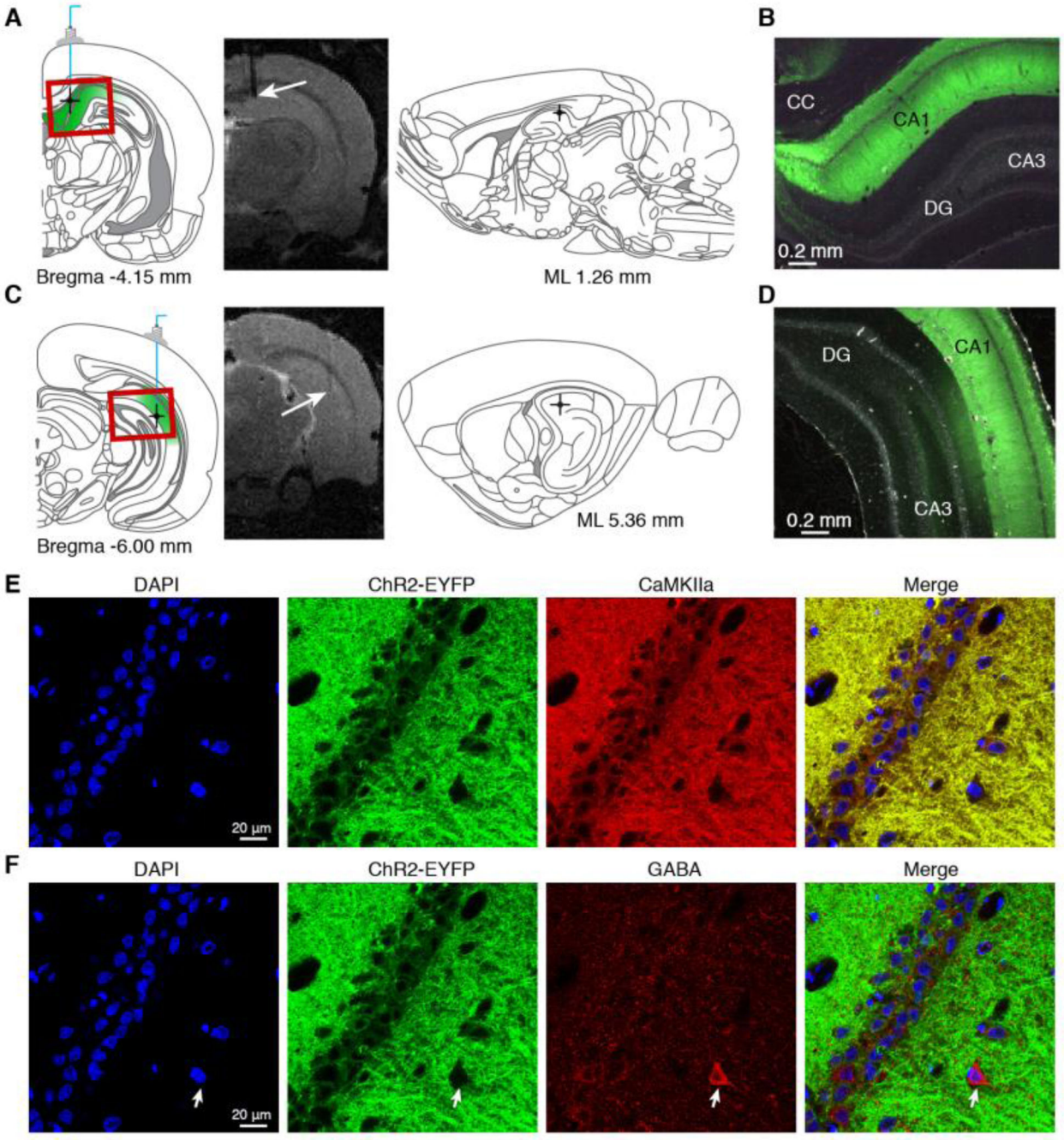

Fig. 1.

Optogenetic targeting of CaMKIIa-positive cells in dorsal (DH) and intermediate (IH) hippocampus. (A,C) Schematic showing average probe locations for DH (A) and IH (C) stimulation. Probe locations were estimated using T2-weighted anatomical scans, as shown for a representative DH- and IH-injected animal. Error bars on atlas schematics represent mean ± SEM across animals. (n = 7 DH-injected, n = 8 IH-injected.). Red rectangles indicate the approximate field of view for micrograph images shown on right. White arrows on representative T2 images indicate the probe location and stimulation site. (B,D)

Fluorescent images confirming ChR2-EYFP expression in the targeted regions. CC: corpus callosum, CA1/CA3: cornu ammonis subfields 1 and 3, DG: dentate gyrus. (E,F) Representative images from immmunohistochemistry confirm the specific expression of ChR2-EYFP in CaMKIIa-positive cells of the hippocampus. Confocal overlays of EYFP with excitatory marker CaMKIIa, inhibitory marker GABA, and nuclear marker DAPI show that CaMKIIa-positive cells (E) but not GABA-positive cells (F) co-express EYFP. The layer of pyramidal cells co-express EYFP and CaMKIIa, but do not stain positive for GABA. The white arrow in (F) indicates a cell expressing GABA, but not EYFP.

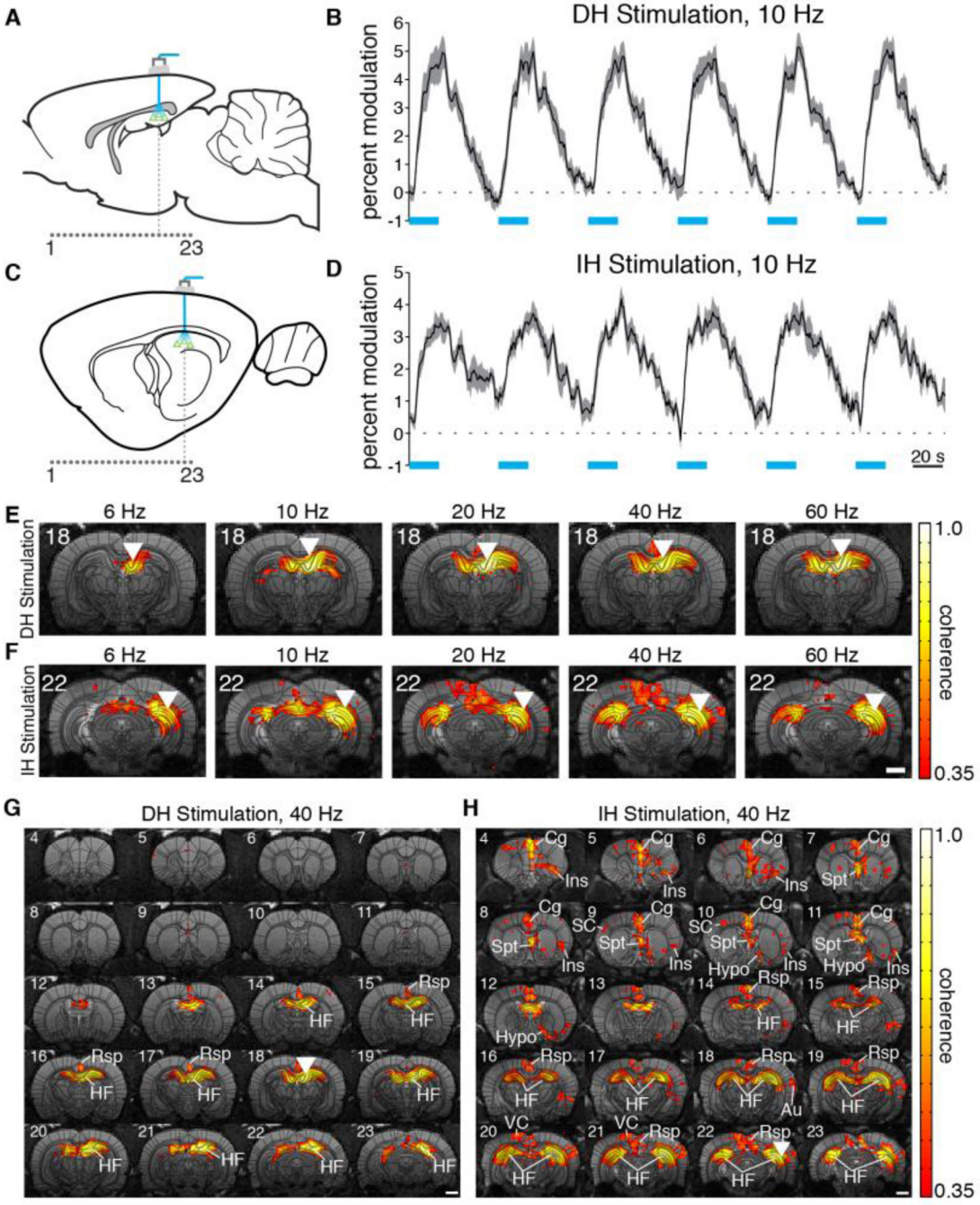

Fig. 2.

ofMRI reveals network-level activity resulting from optogenetic stimulation of CaMKIIa-positive cells in two precise subregions of hippocampus. (A,C) Schematic of transduced cells (triangles), optical stimulation site, and location of acquired coronal fMRI slices (1…23). Slice numbers correspond to activation maps in subsequent figures. (B,D) Representative time series of BOLD signal averaged over active voxels within a 5×5 voxel square at the site of stimulation show that optogenetic stimulation can drive robust responses with 10 Hz, 20 s pulse trains of light (indicated by blue bars). Shaded areas represent one

standard error across animals. (E,F) Robust activation was observed at the site of stimulation across all frequencies and locations tested. The lower tip of white inverted triangles indicates the approximate stimulation location. (G,H) Representative activation maps for 40 Hz stimulations. Activity was mostly restricted to the dorsal hippocampus and retrosplenial cortex during DH stimulation (G), while an extended network of cortical and subcortical regions was recruited by IH stimulation (H). Abbreviations are as follows: Au (auditory cortex), Cg (cingulate cortex), HF (hippocampal formation), Hypo (hypothalamus), Ins (insular cortex), Rsp (retrosplenial cortex), SC (sensory cortex), Spt (septal nuclei), VC (visual cortex). Activation maps are from averaged group analysis images. Scale bars for activation maps are 2 mm. T2-weighted anatomical images are used as underlays in panels E through H.

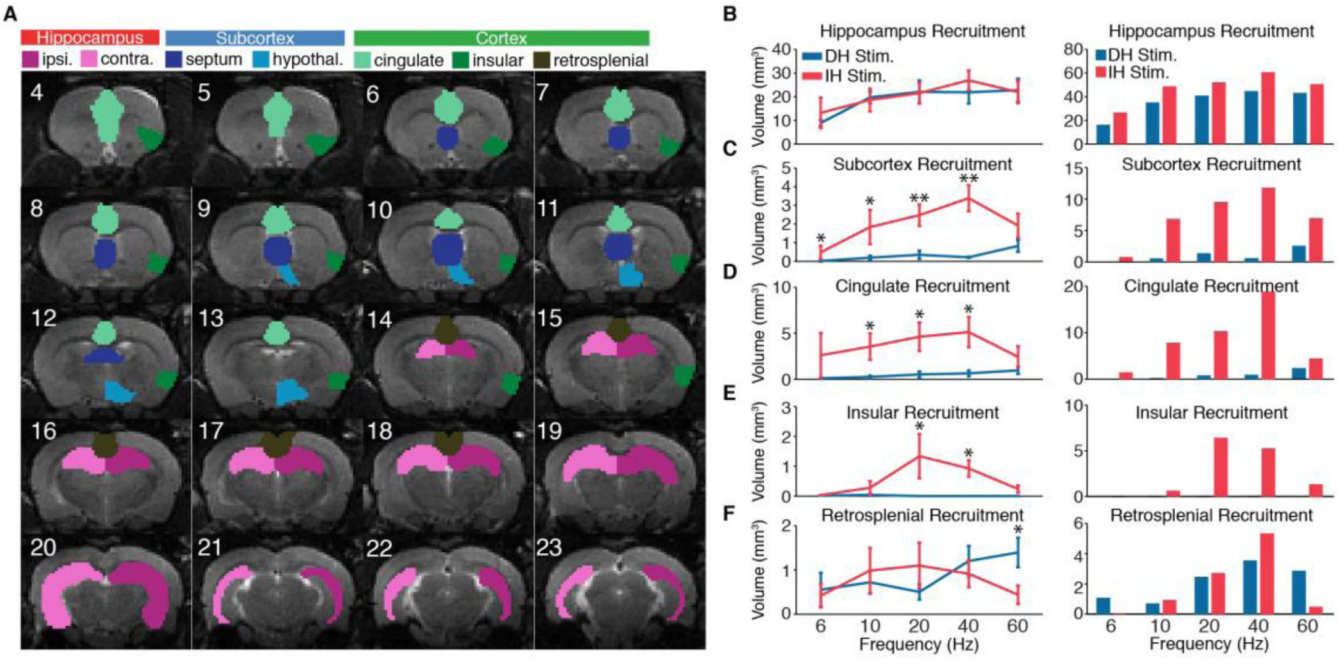

Fig. 3.

Intermediate (IH), but not dorsal (DH), hippocampus stimulation recruits widespread cortical and subcortical networks. (A) ROIs used to quantify activation volume overlaid on T2-weighted anatomical images. (B) Total volume of activation in hippocampus across stimulation locations and frequencies. Error bars on left represent mean ± SEM across animals. No significant differences were observed between DH and IH stimulation. Bar graph on right shows total hippocampal recruitment using group average datasets rather than individual animals. (C). Total activation volume in the subcortical ROI encompassing septal nuclei and hypothalamus. Significantly more volume is recruited during IH stimulation than DH stimulation at 6, 10, 20, and 40 Hz. (D) Significantly more volume in cingulate cortex is recruited during IH stimulation than DH stimulation at 10, 20, and 40 Hz. (E) Significantly more volume in insular cortex is recruited during IH stimulation than DH stimulation at 20 and 40 Hz. (F) Significantly more volume in retrosplenial cortex is recruited during DH stimulation than IH stimulation at 60 Hz. All tests are one-sided Mann-Whitney U Test (* $P < 0.05$, ** $P < 0.005$).

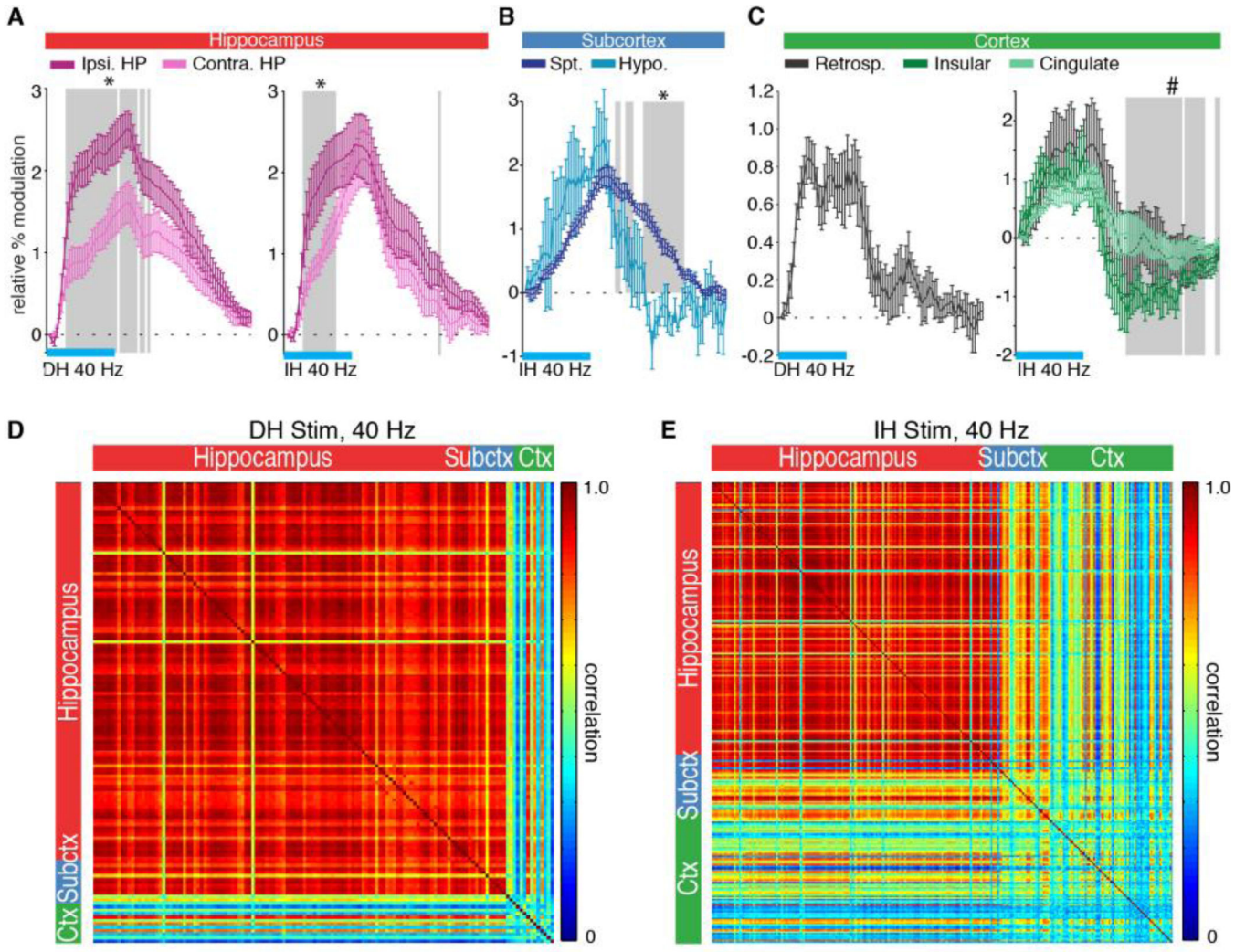

Fig. 4.

Temporal analysis reveals that functionally distinct networks are simultaneously engaged across the brain during DH and IH stimulations. HRFs in (A) through (C) come from active voxels in the ROIs defined in Fig. 3. Error bars represent mean ± SEM across animals. Horizontal blue bars represent the 20 s period of stimulation. (A) During 40 Hz DH (left) and IH (right) stimulation, the contralateral hippocampus shows a delayed response compared to the ipsilateral side. Shaded time points represent indices for which the ipsilateral response is greater than the contralateral response (* $P < 0.05$, one-sided Mann-Whitney U Test). (B) During 40 Hz IH stimulation, the septal nuclei exhibits a sustained response relative to the hypothalamus. Shaded time points represent indices for which the septal nuclei response is greater than the hypothalamus response (* $P < 0.05$, one-sided Mann-Whitney U Test). (C) During 40 Hz DH (left) and IH (right) stimulation, active cortical regions exhibit a much shorter response than hippocampus, quickly decaying upon the end of stimulation. The insular cortex even exhibits a post-stimulus undershoot, during which the HRF is significantly less than zero (shaded time points, # $P < 0.05$, one-sided sign test). (D,E) Cross-correlation matrices for DH and IH stimulation at 40 Hz. Pairwise cross-

correlations were performed over the BOLD time series of active voxels in the prescribed ROIs. DH stimulation results in a mostly homogenous response, confined to the hippocampus. The few active cortical voxels are less correlated with the hippocampal response. During IH stimulation, the multi-region cortical network that is engaged exhibits reduced correlation with the hippocampus, indicating its distinct functional response.

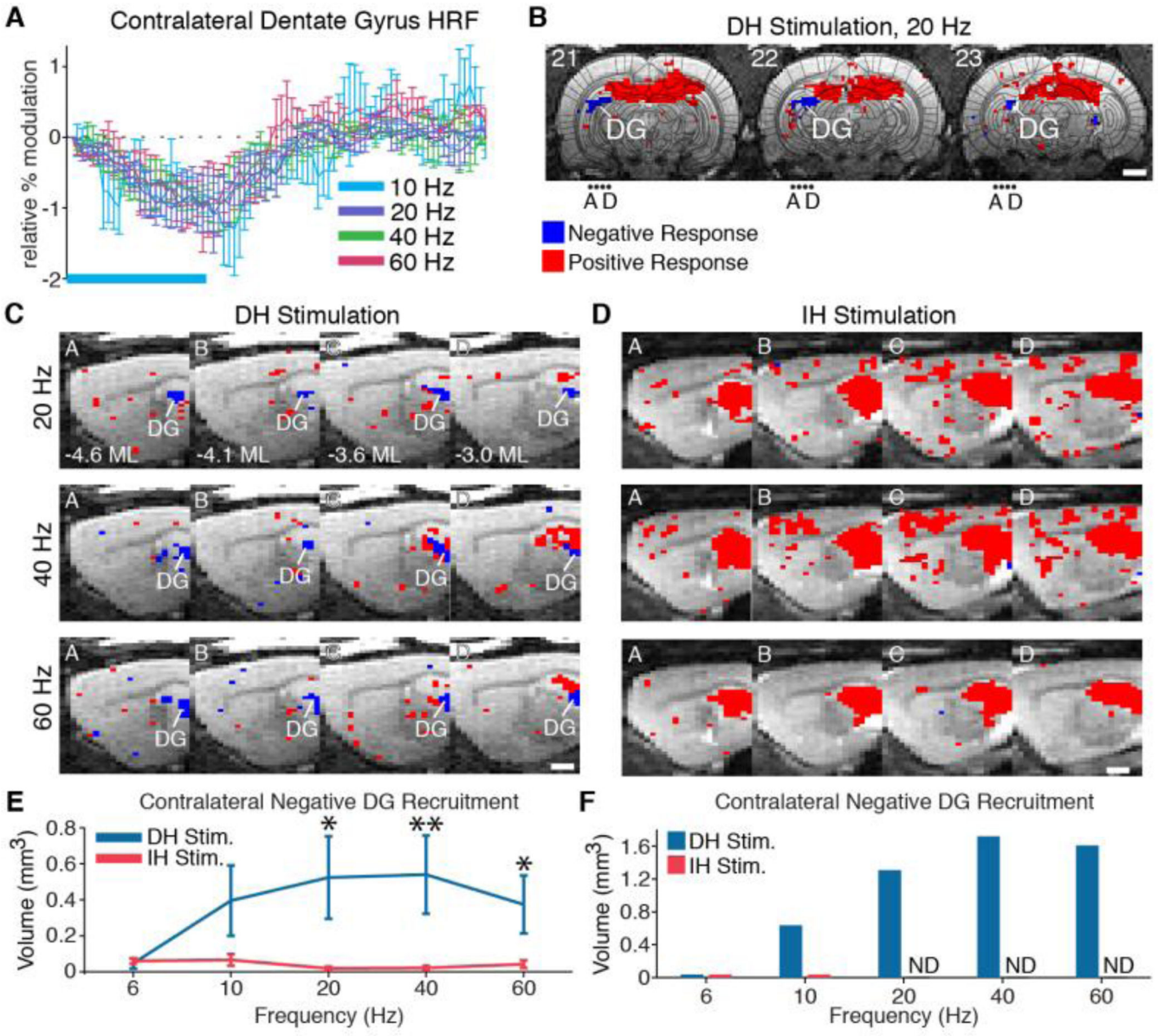

Fig. 5.

The contralateral dentate gyrus exhibits a negative BOLD response during dorsal (DH), but not intermediate (IH), hippocampus stimulation. (A) HRFs of active voxels in the contralateral dentate gyrus that exhibited a negative response during 10, 20, 40, and 60 Hz DH stimulation. Horizontal blue bar represents the 20 s period of stimulation. (B) Representative map shows coronal view of active voxels with positive (red) and negative (blue) responses at the posterior hippocampus during 20 Hz DH stimulation. Negative activity is most pronounced at the dentate gyrus (DG) contralateral to stimulation. Dots labeled A through D indicate sagittal slices shown in *C* and *D*. (C,D) Sagittal view of negative and positive responses in the contralateral dentate gyrus at 20, 40, and 60 Hz for DH and IH stimulation, respectively. (E) Total volume of negative BOLD activity in the contralateral dentate gyrus across locations and frequencies. Significantly more negative

volume was observed during DH stimulation than IH stimulation at 20, 40, and 60 Hz (* $P < 0.05$, ** $P < 0.005$, one-sided Mann-Whitney U Test). (F) Total volume of negative BOLD activity in the contralateral dentate gyrus quantified using group average datasets rather than individual animals. ND: not detected. Activation maps are from averaged group analysis images. Scale bars for activation maps are 2 mm. T2-weighted anatomical images are used as underlays in panels B through D. Error bars in all panels represent mean ± SEM across animals.

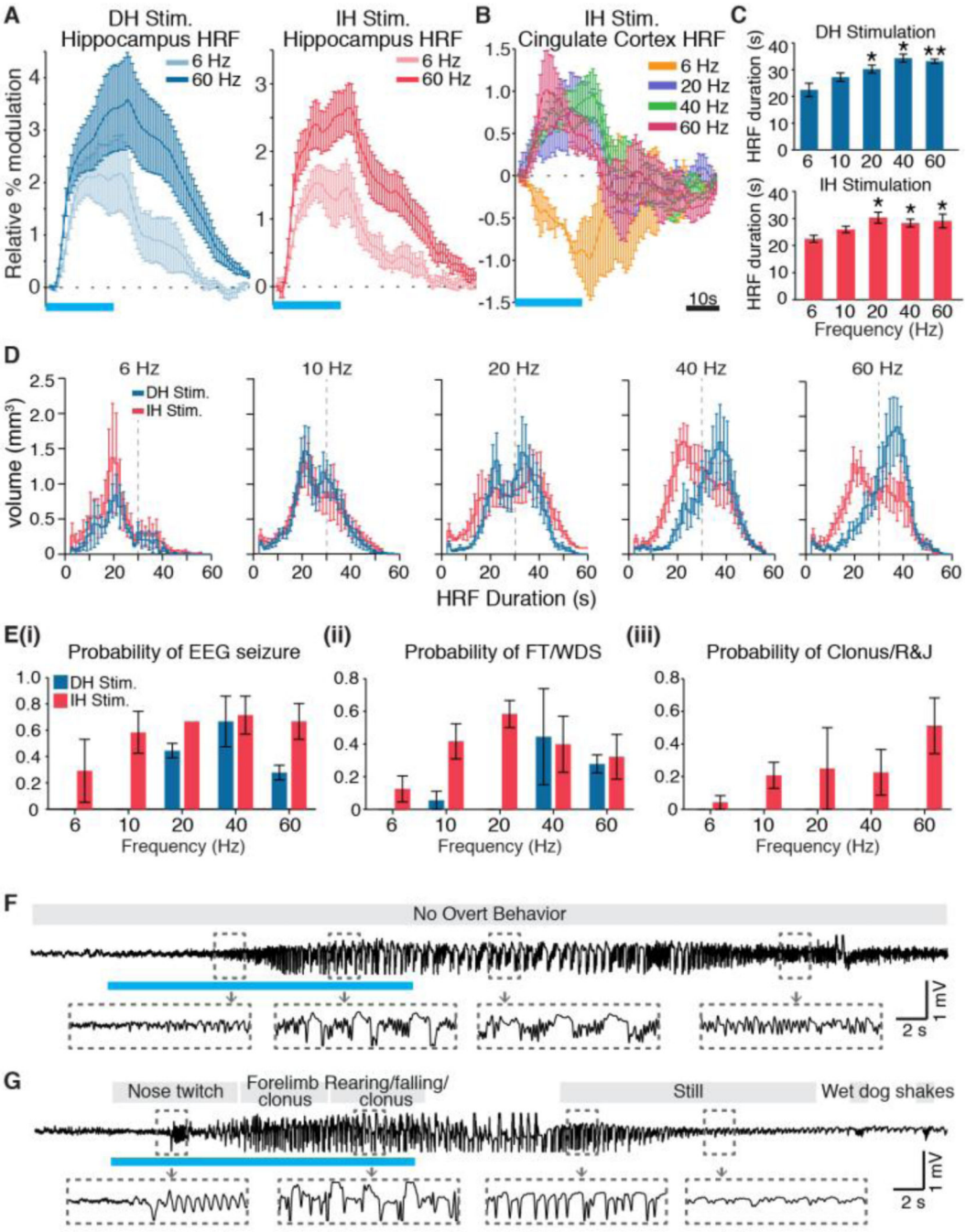

Fig. 6.

ofMRI-revealed dynamics predict seizure-like afterdischarges and behavior. (A) High frequency stimulation results in sustained HRFs in the hippocampus. Representative HRFs at the hippocampus during 6 and 60 Hz stimulation show that the response evoked at 60 Hz is longer in duration for both DH and IH stimulation. (B) HRFs at another region, the cingulate cortex, exhibit an entirely different relationship with frequency, with a negative response at 6 Hz, but positive responses at 20, 40, and 60 Hz. (C) Quantification of the average hippocampal HRF duration. Asterisks indicate frequencies that were significantly

greater than the corresponding 6 Hz case (* $P < 0.05$, ** $P < 0.005$, one-sided Mann-Whitney U Test). (D) Histograms of HRF duration for all active hippocampal voxels show that the distribution of duration increases with frequency for both DH and IH stimulations. (E) *i*. Evolving EEG seizures were observed at all frequencies of IH stimulation, but only at high frequencies of DH stimulation. *ii*. Face twitches (FT) and wet dog shakes (WDS) were observed during stimulation of either location, but were most pronounced and consistent across frequencies for IH stimulation. *iii*. Severe seizure behavior, including clonus and wild running and jumping (R&J), were only observed during IH stimulation. (F,G) Representative EEG traces from DH and IH stimulations at 40 Hz, respectively, show evolving electrographic seizure activity with corresponding behavioral readout. Error bars in all panels represent mean ± SEM across animals. Horizontal blue bars for HRFs and EEG traces represent the 20 s period of stimulation.